Bidirectional Venturi Flowmeter Based on Capacitive Sensors for Spirometry

Laura L. Becerra[1], Tarek Rafeedi[2], Sankaran Ramanarayanan[3], Ian Frankel[3], Juliana Miller[1], Alexander X. Chen[2], Yi Qie[2], Darren J. Lipomi[2], Harinath Garudadri[4], Tse Nga Ng[1]*

[1]Department of Electrical and Computer Engineering, University of California, San Diego
[2]Department of Nano and Chemical Engineering, University of California, San Diego
[3]Department of Mechanical and Aerospace Engineering, University of California, San Diego
[4]Qualcomm Institute, University of California, San Diego
9500 Gilman Drive, La Jolla, CA 92093-0448

*Author to whom correspondence should be addressed: tnn046@ucsd.edu

Keywords: spirometry, capacitive sensor, flowmeter, pressure sensing, respiration

Abstract

In this work, we developed a portable venturi tube capable of measuring bidirectional respiratory flow, and correlated the measurements to pulmonary function. Pressure signals were transduced using flexible and compressible capacitive foam sensors embedded into the wall of the device. In this configuration, the sensors were able to provide differential pressure readings, from which the airflow rate passing through the tube could be extrapolated. Utilizing the venturi effect, the geometry of the spirometer tube was designed through finite element analysis to measure respiratory airflow during inhalation and exhalation. The device tube was 3D-printed and used to measure tidal breathing and deep breathing, along with peak expiratory flow rates, on a healthy individual. This spirometer design allows for easy to use point-of-care diagnoses and has the potential to improve the care of respiratory illnesses.

Introduction

Accurate and in situ measurement of pulmonary function is a crucial aspect of the diagnosis and treatment of chronic respiratory illnesses. Spirometry is a common tool used to measure lung capacity and diagnose respiratory illnesses, such as asthma and chronic obstructive pulmonary disease (COPD).[1,2] Medical grade spirometers that provide real-time continuous breathing data are typically located in hospitals, and thus are limited in access for the public. As a result, use of spirometer devices require referrals from doctors and are typically restricted for patients in immediate acute respiratory distress.[3] When the global healthcare system is under stress, (e.g., the COVID-19 pandemic), access to medical instrumentation can become scarce and pose a bottleneck for medical treatment due to increased demand from the patient side as well as decreased supply from healthcare shortages and supply chain disruptions. Thus, there is a need for low-cost, accessible spirometer devices to increase public access to respiratory diagnostic devices.

The American Thoracic Society and European Respiratory Society have established international standard for spirometry devices to ensure suitability for clinical grade pulmonary function tests (PFTs).[4] Among the recommended measurements, one of the most useful values is the peak expiratory flow rate (PEFR), which is the maximum flow rate achieved from a forced full exhalation. PEFR measurements are one of the most important and widely used tests for PFTs, as they provide information regarding constriction in major lung passages and minute bronchus branches.[5,6] This spirometric index is widely used to monitor and diagnose COPD and, more commonly, asthma.

Spirometers are generally categorized as either volumetric or flow-measuring.[7] Volumetric spirometers measure lung capacity by quantifying the inhaled and exhaled volume of air, while flow-measuring spirometers measure the air velocity of the exhaled and inhaled air. Volumetric spirometers are generally low-cost but are primarily used as incentive spirometers. Incentive spirometers use a piston that moves based on the volume of air exhaled into the spirometer. Thus, volumetric spirometers are typically used to help patients with asthma[8] or those recovering from a surgery[9] reach a target volume, as it allows them to watch the piston move closer to a target volume as they breathe forcefully. Conversely, flow-measuring spirometers are capable of obtaining multiple spirometric indices, providing more useful information for disease monitoring and diagnoses. Flow-measuring designs include turbine sensors, hot-wire anemometers, and ultrasonic flowmeters.[10–13] While many of these architectures have been validated, there are advantages and disadvantages to a given sensing mechanism. For example, ultrasonic and hot-wire anemometry flow detection are generally costly and require complex calibration.[14] Differential pressure-based spirometer designs are potentially inexpensive and portable, however, most studies run into the limitation of measuring flow rates in one direction only.[15] For example, Zhou et al. developed a wireless pneumotachometer, which measured differential pressure across a flow restrictor in a configuration known as the Lilly-type sensing unit, but the system was limited to only measuring positive flow rate (exhalation) values.[16] Flow-restricting designs also require more maintenance, since the restrictors need to be replaced as particulates from the breath build up from use. Alternatively, face masks have also been used with embedded triboelectric nanogenerators for real time respiration measurements[17,18]. Other designs, such as the venturi tube, were limited to measuring flow rate for exhaled air,[19,20] and only used to compare lung function between individuals with and without COPD.[21]

The venturi tube is a widely used device to measure the flow rate of a fluid passing through the tube[22]. Outside of respiratory measurements, the venturi tube is seen in several consumer products such as industrial vacuum cleaners, atomizers, wine aerators, clarinets, among many others.[23–26] The venturi design approach for spirometry specifically was originally evaluated by Titheradge and Robergs in a study that tested the performance of the venturi design under static and dynamic conditions.[27] A pneumotachometer and turbine flow sensor were used in series with the venturi meter, as reference measurements. In this configuration, the authors were able to compare signal-to-noise ratio (SNR), response time, air fluid-state transitions, and other device characteristics between the connected spirometers using paired t-tests. Overall, the authors found no significant difference in signal quality or response time between the venturi meter and the pneumotachometer. However, they observed that at lower air velocity and flow rates ($< 0.5\ \mathrm{L\ s^{-1}}$), there was distortion in the differential pressure readings because of transitions between laminar and turbulent states of flow. This overestimation was attributed to the fact that the flow could not reach a steady state of full turbulence in the venturi flow meter. Barring this limitation for lower flow rates, the venturi design was deemed adequate to detect parameters attributed to respiration by normal humans. However, one of the disadvantages of a venturi flowmeter is its limitation to unidirectional measurement. This unidirectional constraint is due to complications with flow separation at the divergent sections of the tube. Divergent geometries can cause chaotic flow separation at high Reynolds numbers, which would exert unsteady pressure on the pipe walls and yield unreliable, fluctuating measurements. Given this performance evaluation of venturi tubes as spirometer devices, in this work, we designed a bidirectional venturi tube to measure respiratory flow rate via differential pressure measurements for both inhaled and exhaled air in human respiration.

Experimental Methods

Spirometer design

A common way to calculate fluid flow through a tube utilizes Bernoulli's principle on fluid flow. This principle states that a fluid exerts less pressure on its surroundings when it is flowing at a faster rate compared to a slower rate.[22,28] The venturi effect can be used to experimentally estimate internal fluid flow through a constriction using Bernoulli's principle for a fluid with a known density . This principle assumes the fluid is both inviscid and incompressible (i.e. neglects viscous/friction losses and fluid compression).

In this work, we designed a symmetrical venturi tube of a slender geometry with three sensing points to measure air flow in both directions (**Figure 1a)**. The pressure transducers are embedded into the tube walls to avoid obstructions to air flow. To measure respiratory exhalation, the differential pressure measurement was taken between sensors S1 and S2, with the assumption that there was minimal flow separation moving from the mouthpiece inlet to sensor S2. During this time, sensor S3 would experience chaotic flow due to separation and, consequently, was not used in the measurement. Flow analysis, as discussed later in this section, indicated that the flow over sensor S3 would have sufficient time to settle before the inhalation measurement. During inhalation, the pressure drop was measured between sensors S3 and S2, while flow separation was present at sensor S1 but would likewise dissipate before the subsequent exhalation in the next breathing cycle.

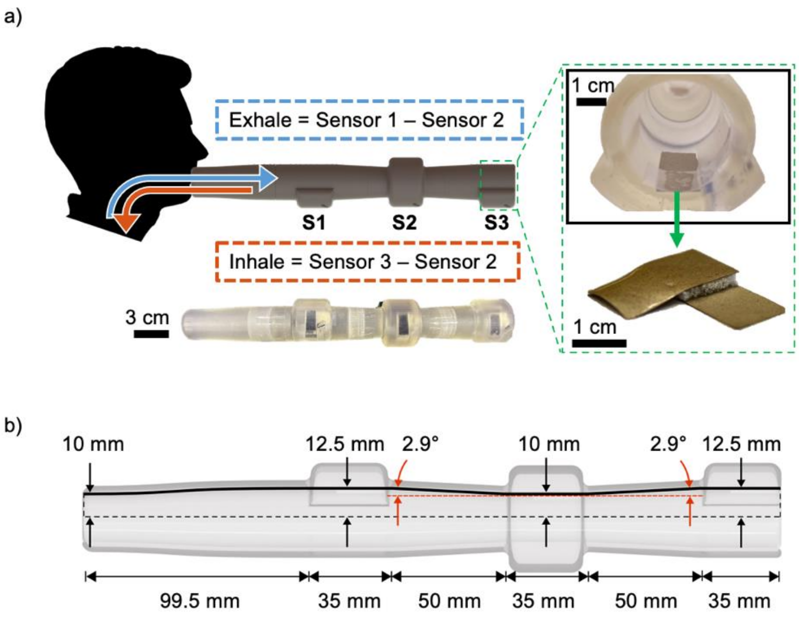

Figure 1. Overview of the bidirectional venturi spirometer. **a)** User inhaling and exhaling into the tube. The blue line represents exhalation which is measured by subtracting the pressure of sensor S2 from the pressure of sensor S1. The orange line represents inhalation, which is measured by subtracting the pressure of sensor S3 from the pressure of sensor S2. The 3D-printed spirometer tube is embedded with S3 capacitive foam sensors in the tube wall. The green box shows the embedded sensor inside the tube wall with a close-up picture of the capacitive sensor. **b)** Spirometer dimensions.

The conservation of mass, for constant density internal fluid flow, dictates that the volumetric flow rate (Q in m^3 s^{-1}) through a tube is equivalent to the velocity (v in m s^{-1}) of the flow multiplied by the cross-sectional area of the tube (A in m^2), where the subscripts indicate the tube segments:

$$Q = v_1 A_1 = v_2 A_2 = v_3 A_3 \qquad (1)$$

$$p_1 - p_2 = \frac{\rho}{2}\left({v_2}^2 - {v_1}^2\right) \qquad (2)$$

$$Q = A_1 \sqrt{\frac{2}{\rho} \cdot \frac{(p_1 - p_2)}{\left(\frac{A_1}{A_2}\right)^2 - 1}} \qquad (3)$$

The pressure drop at the constriction was measured in the venturi tube and calculated according to Bernoulli's principle (Eqs. 1 and 2). The differential pressure $p_1 - p_2$ (in units of Pa or N m^{-2}) was proportional to the difference in the squares of the velocities. The fluid density (ρ) of this system was approximated as the density of air, 1.22 kg m^{-3}. Equation 3 was derived from Equations 1 and 2 to calculate the ideal exhalation volumetric flow rate using the cross-sectional areas and pressure drops; a constant of 1000 (not shown in Equation 3) was applied for unit conversion from m^3 s^{-1} to L s^{-1}. Since the flow direction is reversed for inhalation, Equation 3 was multiplied by -1 to denote inhalation data. For a continuous flow rate profile, whenever $p_1 - p_2$ was positive, it was used as the differential pressure signal to calculate the flow rate. On the other hand, when $p_1 - p_2$ was negative, $p_3 - p_2$ was used as the differential pressure signal for the flow rate calculation. The negative differential pressure signals were discarded in the calculation of the flow rate. Simulation-based correction factors are applied to the pressure (S_p) and flow rate (S_f) values, as elaborated on later in the discussion section.

To enable bidirectional measurements, we designed this system assuming unidirectional flow for inhalation and exhalation individually. This condition could be met by choosing a tube geometry that was as slender as possible, illustrated in **Figure 1b**. To mitigate flow separation and consequently unstable pressure measurements at the sensor locations, the changes in diameter were minimized, decreasing from 25 mm at the inlet/outlet cross-sections (locations of sensors 1 and 3) to 20 mm at the constricted section (location of sensor 2). Likewise, the transition in diameter was minimized and fileted with a 2.9° angle in the interior. Past the inlet, the tube was made symmetric about the central sensor to allow for the measurement of airflow in both directions. The three sensors were placed equidistant from each other and centered in each fixed-diameter section. The dimensions of the tube was optimized in simulations to maximize sensor pressure changes in each direction.

To assess the viability of the bidirectional measurements, another consideration was the Reynolds number (Re),[29] which is the ratio between the inertial and viscous (frictional) forces of the fluid. The Reynolds number was calculated using Equation 4:

$$Re = \frac{\rho u L}{\mu} \tag{4}$$

where ρ is the fluid density (kg m^{-3}), u is the flow speed (m s^{-1}), L (m) is the characteristic linear dimension, and μ (kg m^{-1} s^{-1}) is the dynamic fluid viscosity. The density and dynamic viscosity

(1.849×10^{-5} kg m^{-1} s^{-1}) were approximated to be that of air at room temperature for human respiration.[30] The characteristic linear dimension (L) was approximated to be the diameter of the tube inlet, which was 20 mm. Human exhalation has been reported to range in velocity from approximately 2 m s^{-1} up to 10 m s^{-1}.[31] These parameters yielded Reynolds numbers of 2,600 and 13,200, respectively. Other studies have suggested a laminar-turbulent transition Re values of 2300 and 4000, with an $Re > 4000$ implying fully turbulent flow.[32] At high Re values, the fully developed turbulent state creates a boundary layer with more inertial force near the wall compared to viscous force, making it harder to separate. Because of the gradual changes in diameter and high Re values at higher flow rates, the flow did not separate early in the convergent sections. Even if separation did occur, it would be limited to a small region inside the tube as opposed to conditions outside the tube, which could cause much more disruption. As such, we expect some unstable pressure measurements for lower velocity breathing (tidal breathing) and stable measurements for higher velocities (deep breathing and PEFR measurements).

The third consideration made was the consideration of the Strouhal number (St), which describes the mechanism of flow oscillations:[33]

$$St = \frac{fL}{u} \tag{5}$$

where the characteristic length is the same value as the linear dimension (L) used in Equation 4. The vortex shedding frequency (f) of this system was assumed to be 0.25 Hz (a rate of 15 breaths per minute), as the typical respiration rate for adults is between 10 and 20 breaths per minute[34]. The flow velocity range of human exhalation (2 m s^{-1} – 10 m s^{-1}) yields Strouhal numbers of 2.5×10^{-3} and 5×10^{-4}, respectively. Such low magnitude Strouhal numbers associated with human breathing indicates that the flow developed at any given time reached quasi-steady state. For this reason, we determined that one flow direction can be assumed to have no impact on the other, thus allowing our venturi spirometer to operate bidirectionally. The resulting spirometer design was realized with a stereolithography three-dimensional (3D) printer in combination with additive fabrication techniques as explained below.

Sensor Fabrication Materials

Ag/AgCl ink (Ercon), Sylgard 184 poly(dimethylsiloxane) (PDMS) (Dupont), PELCO fast drying silver paint (Ted Pella Inc), NaCl, and 28 AWG shielded twisted pair cable (Amazon) were used to fabricate the capacitive foam sensors.

Sensor Fabrication

The capacitive foam sensors were reproduced from a work by Zhai et al.[35] The electrodes were fabricated on a 75 mm x 50 mm glass slide sprayed with mold release spray (Smooth-On). First, two thin pieces of 100 μm thick aluminum tape were adhered to each longer side of the slide, leaving the slide area between the tape pieces bare. Poly(dimethylsiloxane) (PDMS) (Sylgard 184, 1g, 10:1 ratio of PDMS:curing agent) was prepared and left under vacuum for 5 min to remove air bubbles, while the mold release spray was left to dry. The PDMS mixture was then blade coated onto the prepared glass slide to create a 100 μm thick layer of PDMS. This film was cured on a hotplate for 30 min at 90 °C. The 10:1 PDMS mixture was mixed with Ag/AgCl ink (Ecron) at a ratio of 7:1 (Ag/AgCl ink: PDMS mixture) for forming flexible conductive electrodes. On each of the long sides of the glass slide, five additional pieces of silver tape were put down to make a confinement wall with an overall thickness of 500 μm above the underlying PDMS layer. The (Ag/AgCl):PDMS mixture was left under vacuum for 10 min then blade coated on top of the partially cured PDMS layer on the slide. This film was then cured on a hotplate for 1 h at 100 °C. Once cured, an X-Acto knife blade was used to cut along the edges between the tape and electrode area, and the electrode sheet was carefully peeled from the slide, from which smaller electrodes (1 cm x 2 cm) were cut.

To make the porous foam dielectrics, PDMS (1 g, 10:1 ratio of PDMS:curing agent) was prepared and mixed with sodium chloride (NaCl) in a 17:20 ratio (85 wt% NaCl/PDMS). Once well mixed, the mixture was poured onto a 75 mm x 50 mm x 1 mm mold and cured on a hotplate for 30 – 60 min at 90 °C. Then, the cured mixture was removed from the mold and submerged in a dish filled with deionized (DI) water for 24 h to leach out the NaCl. The DI water was replaced the following day and again left overnight for a total of 48 h. The following day, the PDMS foam was warmed on a hotplate at 80 °C to evaporate the DI water from the foam. Once all water was evaporated, the foam was cut into 1 cm x 1 cm squares.

To assemble the sensors, one silver electrode was placed on a glass slide with the PDMS encapsulation layer facing down. A small amount of 10:1 PDMS mixture was placed in a 1 cm x

1 cm area on the electrode and a PDMS dielectric foam was placed on top of the PDMS mixture. This structure was cured on a hotplate at 90 °C for 30 minutes. Once cured, another silver electrode was placed on the glass slide, with the PDMS encapsulation layer faced down, and another small amount of the PDMS mixture was placed in a 1 cm x 1 cm area on the electrode. The other side of the dielectric was placed on top of the PDMS mixture, sandwiching the foam dielectric between the two electrodes. This device was cured for an additional 30 min at 90 °C.

To form electrical connections, a shielded twisted pair of 28 AWG wires was stripped to expose the two metal wires. Each wire was contacted and adhered to a silver electrode of the sensor using fast-drying conductive silver paint (Ted Pella, PELCO). The paint was cured on a hotplate at 90 °C for 5 min. A small amount of 10:1 PDMS mixture (PDMS/curing agent) was painted on top of this connection and on the rest of the exposed contacts of the silver electrode. This process was repeated for the second exposed wire to connect the other silver electrode on the capacitive sensor.

Spirometer tube fabrication

The spirometer tube was 3D printed using a resin 3D printer (Form Labs, Form 3). The tube design was printed using a photopolymer resin (Clear V4). The print was cured at 60 degC for 15 minutes, which are the recommended curing conditions to fully cure the resin and non-toxic.

Results and Discussion

Characterization and Calibration of Capacitive Sensor

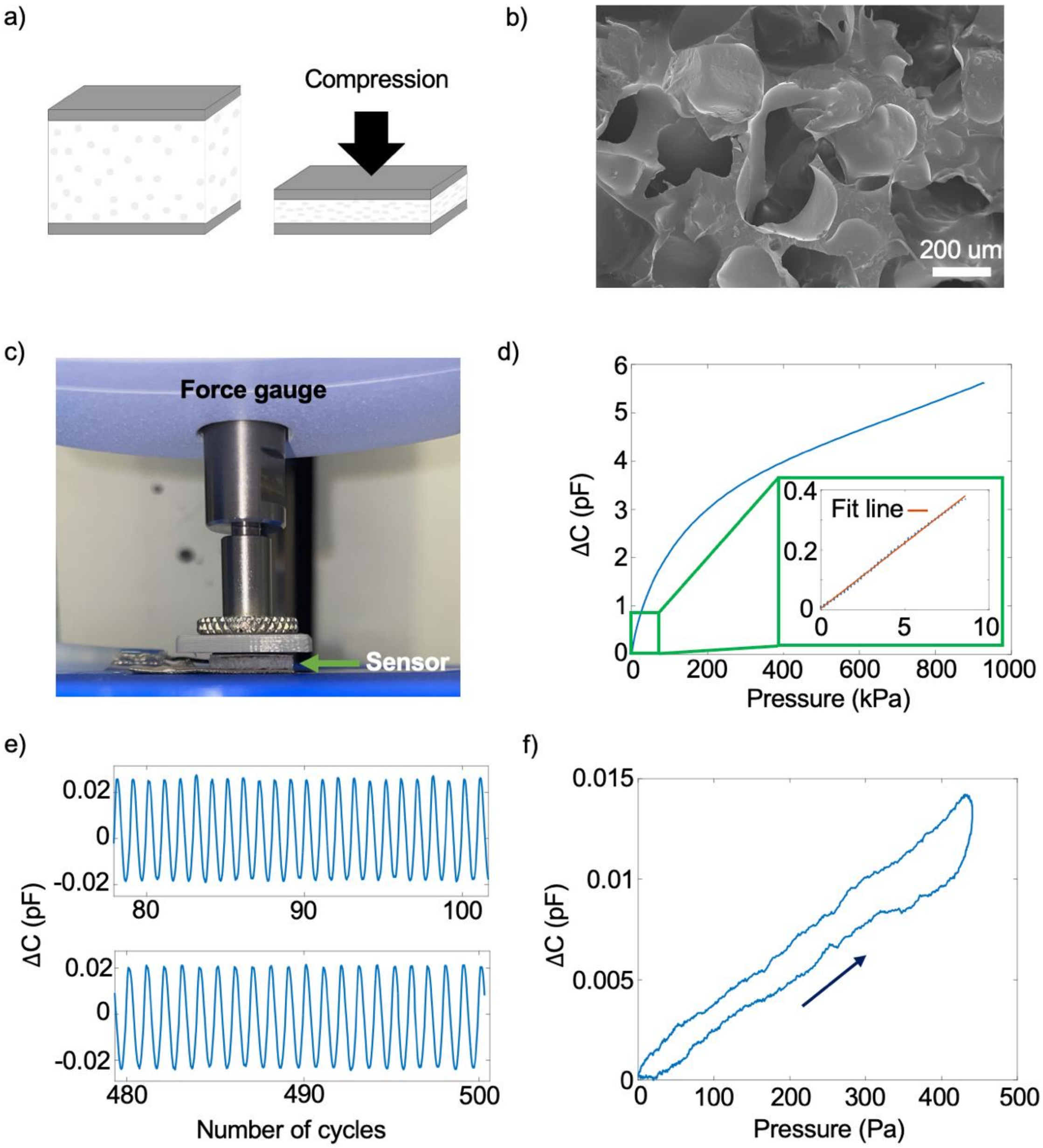

Figure 2. Mechanical characterization and calibration of capacitive sensors. **a)** Diagram of capacitive foam sensor under compression. **b)** SEM image of PDMS dielectric foam cross section. **c)** Photograph of a sensor underneath a force gauge for compression measurements **d)** Calibration curve showing the change in capacitance (instantaneous capacitance minus baseline capacitance) as a function of compression pressure. The green box shows a zoomed-in plot of the low-pressure

regime with the corresponding fit used to determine a capacitance-to-pressure conversion factor. **e)** Cyclic compression of the pressure sensor. The top plot shows the capacitance during the 80th - 100th cycles and the bottom plot shows the response during the 480th-500th cycles. f) Capacitance as a function of pressure for one compression cycle, showing slight hysteresis in the sensor readout.

The capacitance-to-pressure conversion was calculated using compression measurements using a Mark-10 force gauge (**Figures 2a-2c**). The linear regime (<10 kPa) of the pressure-capacitance plot was used for the calculation of the capacitance-to-pressure conversion (**Figure 2d**). After comparing multiple sensor calibration curves, we used the most common trendline slope for the linear regime. The sensor was compressed cyclically to 400 Pa, and a very small drift of 0.3 fF was observed over 500 compression cycles (**Figure 2e**). We also looked at 1 compression cycle to calculate sensor hysteresis (**Figure 2f**). The hysteresis effect was found to be approximately 43% at 100 Pa and decreases to approximately 28.5% at 400 Pa. The change in pressure observed for tidal breathing falls in the <250 Pa range, while PEFR and deep breathing measurements yield pressures up to 1 kPa. Therefore, we expected to see more uncertainty in the tidal breathing measurements due to the hysteresis effect.

As moisture accumulates from human breath inside of the spirometer, we looked at sensor stability before and after humidity exposure for 30 minutes. The humidity of human exhaled breath has been reported to range from 41.9% to 91.0%.[36] After exposing our sensors to 50-88% humidity, we saw negligible changes as shown in **Figure S1**. The small, reported differences in sensor readout with and without humidity exposure justified use of this sensor in the device as it can withstand moist conditions. Lastly, we also looked at sensor response time via a ramp compression experiment one two different sensors (**Figure S2**). The delay in reaching the peak capacitance after reaching peak compression for the two sensors was 148 ms and 563 ms. As a full cycle of breathing is typically from 2.5 – 3.5 seconds, the response delay can be from 14-20% of a full breathing cycle, which is an important factor to consider when looking at output breathing signals.

Simulations of Respiratory Flow Rate Characteristics through Finite Element Analysis

In order to calculate the expected response of the pressure sensors, Finite Element Analysis was performed using the acoustics module in COMSOL Multiphysics v5.6. An acoustic module was chosen given the oscillating profile of the input signal (breathing cycles). The interior wall of the tube was set as a hard boundary. The outlet of the tube was treated as an open boundary to atmosphere, and was given an impedance value of 420 (Pa·s) m^{-1} for air at standard temperature and pressure. The mouthpiece of the tube was given a harmonic flow rate profile with a frequency that matched previous data sets for breathing.[37] The simulation was run for an airflow period of 12 seconds, and the pressures at the locations of the 3 sensors were recorded and exported to MATLAB R2021a for post-processing.

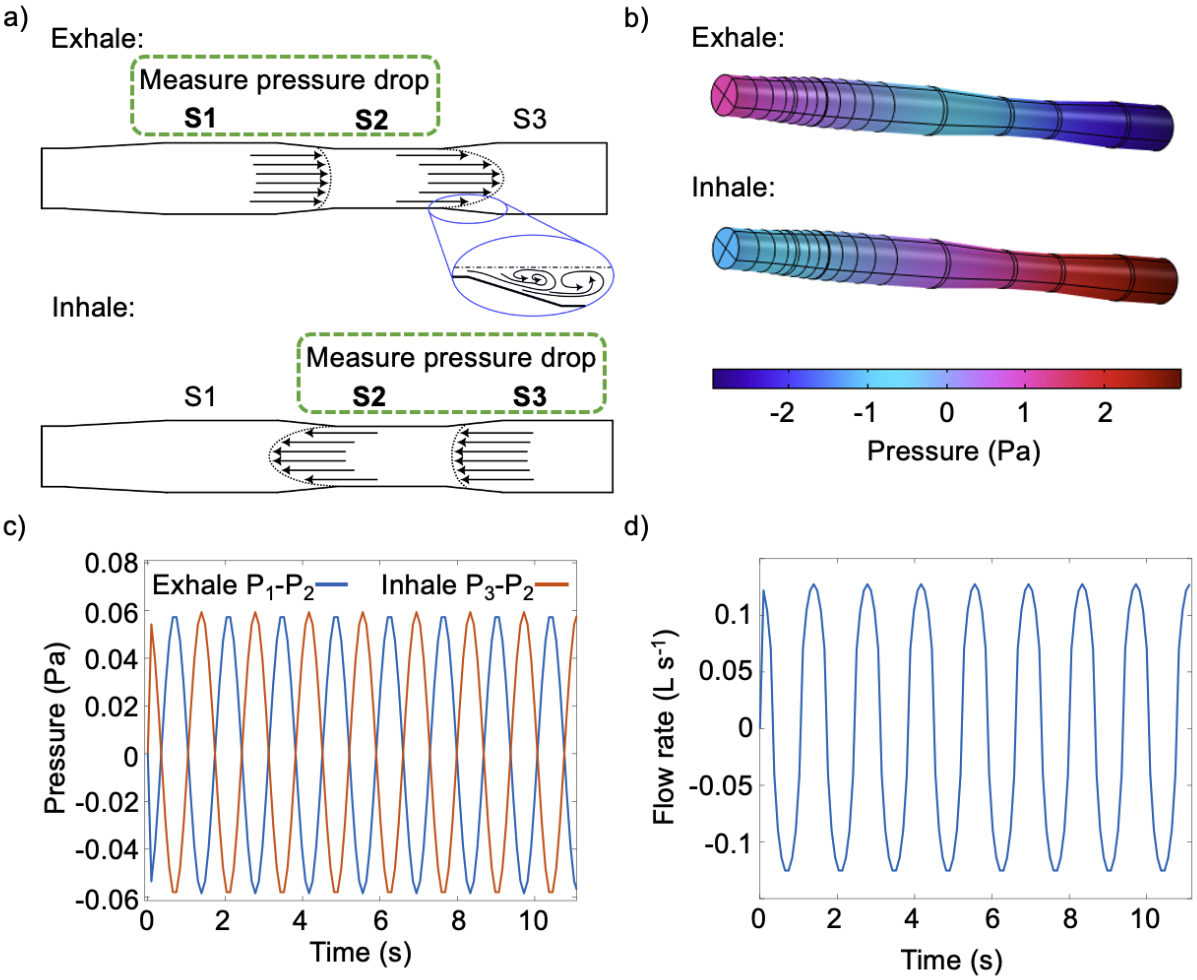

Figure 3. Simulated respiration flow behaviors. **a)** 2D pressure profiles along inner walls. **b)** 3D simulation of pressure for inhale and exhale time points, which are the minima and maxima of the inlet flow rate profile, respectively. **c)** Differential pressure signals (orange and blue) at the sensor locations. The exhale signal (blue) is the signal of sensor 2 subtracted from that of sensor 1, while the inhale signal (orange) is the signal of sensor 2 subtracted from that of sensor 3. **d)** Flow rate plotted over time calculated from differential pressures in b.

The local pressure inside the venturi tube showed the pressure decreasing from the inlet to the outlet for the exhale and the opposite trend for the inhale, validating that we should see a pressure drop for the 2 sensors in each respective direction (sensors 1 and 2 for exhale and sensors 2 and 3 for inhale) (**Figures 3a** and **3b**). The differential pressure at the sensors was calculated for exhalation and inhalation (positive and negative flow at the input, respectively) for tidal breathing (**Figure 3c**). The exhale signal (blue line) was sensor 2 pressure signal subtracted from sensor 1, and the inhale signal (orange line) was sensor 2 signal subtracted from sensor 3. The inhalation and exhalation sinusoidal peaks in **Figure 3c** were 180 degrees out of phase from each other, as inhalation stopped once exhalation started and vice versa. The average peak-to-peak amplitude for tidal breathing from previous studies was approximately 0.1 L s^{-1}.[38] We chose to emulate tidal breathing in this simulation based on the amplitude of the input flow rate profile of this same value (0.1 L s^{-1}). Finally, the venturi flow **Eq. 3** was then used to calculate the flow rate from the differential pressure values (**Figure 3d**).

The FEA simulation calculated the flow rate at the sensor locations for a range nominal inlet flow rates (0.1 L s^{-1} and 2–6 L s^{-1} in step of 1 L s^{-1}). As demonstrated in **Figure S3a**, we found a discrepancy between the nominal input flow rate and the calculated flow rate at the sensor locations. The discrepancy is possibly due to the fact that an acoustics module was used, rather than a computational fluid dynamics (CFD) module. The acoustics module assumes compressibility of the fluid, while Bernoulli's principle in Equation 3 does not, likely causing an underestimation of pressure at the sensor locations due to variable fluid density throughout the tube (**Figure S4**). The fitting function comparing the nominal flow rates to the calculated flow rates was found to be

$$y = 6.1527x^2 + 5 \times 10^{-6}x + 3 \times 10^{-7}\,, \qquad (6)$$

where x represents the flow rate from the pressures at the sensor locations and y represents the nominal flow rate. This equation was used to convert the flow rate calculated from the sensor pressures measured in the device to the nominal flow rate, using Equation 6 to obtain the adjustment factor S_f as explained in the Supplementary Information.

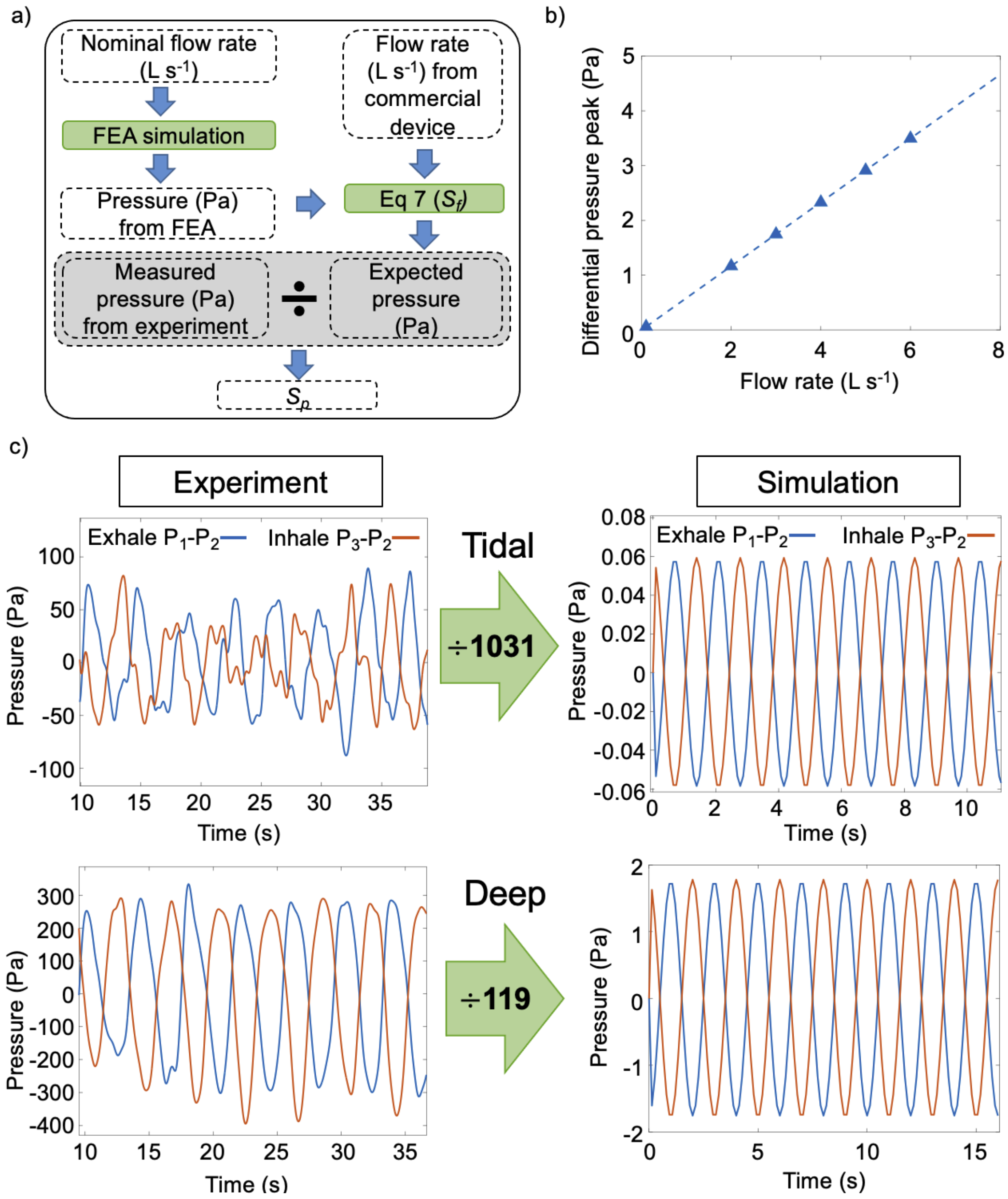

Figure 4. Pressure scaling factor calculations. **a)** Flow chart for finding the differential pressure scale factor S_p. **b)** Differential pressure peaks as a function of nominal flow rate with dashed trendline. **c)** Rows 1 and 2 correspond to tidal and deep breathing, respectively. The plots on the left show the differential pressure waveforms as gathered from experimental measurements, while the plots on the right show the differential pressure waveforms calculated from simulations. The scaling factors are shown in the green arrows in between the left and right plots.

The pressure values were calibrated to match those of the expected flow rates for the respective breathing types in simulation (tidal, deep, and forced), following steps shown in the flowchart of **Figure 4a**. The trendline for the relationship between peak pressure and nominal flow rate is shown in **Figure 4b**. The linear fit line from this plot is:

$$y = 0.5827x \tag{7}$$

where x is the nominal flow rate in L s^{-1} and y is the pressure peak in Pa.

For tidal breathing, the pressure values were scaled to those simulated using a flow rate of 0.1 L s^{-1}, based on previous literature reports for tidal breathing.[38] Our data thus this required a scaling factor S_p of 1,031 (using Equation 7) to get peak pressure values of ~0.05 Pa, matching the peak pressure value for tidal breathing simulations (**Figure 4c)**. The same scaling method was used to calculate the scaling factors S_p for deep breathing (119) and PEFR (158) measurements (**Figure S5**). The only difference is that the simulation flow rates did not include the high PEFR flow rate measured from a commercial spirometer. The differential pressure peaks, therefore, were extrapolated for higher flow rates to include the PEFR measurement range in order to calculate the scaling factor for PEFR measurements (**Figure 4b**). Together the scaling and adjustment factors, yielded results matching simulation and reasonable ranges to match commercial device readings for deep breathing and PEFR values, elaborated on further in the discussion section.

Breathing Tests

The spirometer was tested on a healthy individual for three different types of breathing exercises: tidal, deep, and peak expiratory flow. To reduce germ contamination and as an extra precaution for ensuring no contact with toxic materials, we covered the mouthpiece of the device with 3M Tegaderm film. We also wiped down the interior of the tube with an antiseptic wipe prior to use. For data analysis processing, the first step consisted of smoothing the capacitance data in the three sensors (**Figure 5a**). The corresponding differential pressure values were then calculated after the capacitance (pF) was converted into pressure (Pa), for which only the positive portions of each inhale and exhale signal were used in the flow rate calculation (**Figure 5b**). The negative portions of the respective signals were discarded, as these indicated timepoints at which flow separation was occurring. The exhalation and inhalation waveforms were separated by a phase shift of 180°, as predicted in the COMSOL simulations. Finally, the corresponding flow rate was calculated from the differential pressure values (**Figure 5c**). The calculated flow rates were higher than the values shown in **Figure 3d**, because these data corresponded to measurements taken while deep breathing, while the simulations in **Figure 3d** were given input parameters for tidal breathing.

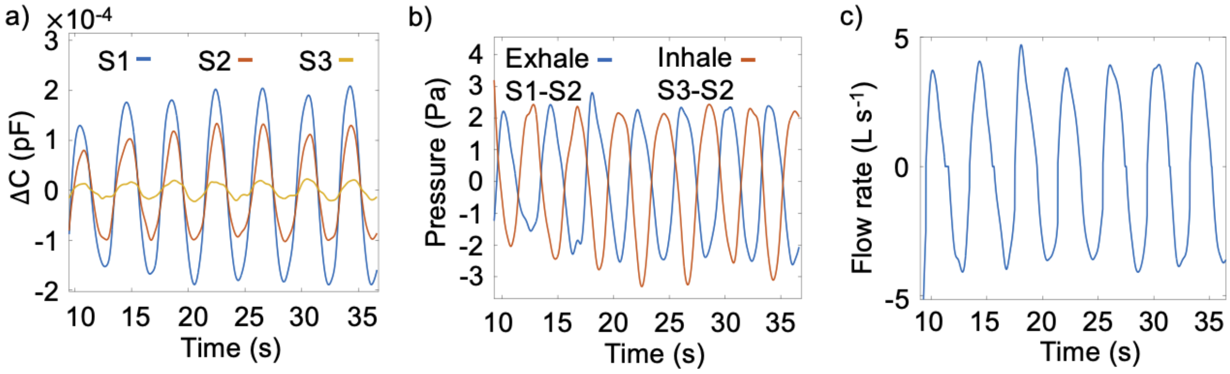

Figure 5. Respiratory airflow output. **a)** Plot of capacitance over time for all three sensors during deep breathing. **b)** Differential pressure waveforms for deep breathing, calculated from the plot in a. **c)** Corresponding flow rate over time, calculated from the waveforms in part b using Equation 3.

Figures 6a—6c shows flow rate as a function of time for tidal breathing, deep breathing, and a PEFR measurement, respectively. Flow volume loops for each breathing type were calculated by integrating the flow rate over time. The flow rate obtained from the differential pressure signals was negative in value for inhalation and positive for exhalation.

In general, tidal breathing cycles show that the subject did not inhale and exhale the same volume of air within each cycle. Therefore, the start and end points of the flow volume loops were often offset. This offset is due to the inability for human subjects to exert precise control over their breathing volume in shallow tidal breathing. Some of the mismatch between cycles is also likely due to distortion from the laminar-turbulent fluid transition at low flow rates during tidal breathing[39], as well as hysteresis of the sensor. The observed hysteresis implies that pressure values recorded during decompression were higher than expected, as it took longer for the sensor to return to its zero state. The higher uncertainty from hysteresis for the tidal breathing regime, in conjunction with the laminar-turbulent fluid transition (*Re* = 2300-4000) occurring more frequently for tidal breathing flow rates, yielded less accurate measurements, a result in agreement with those Titheradge and Robergs[39]. Some tidal breathing measurements also show flat line regions on the x-axis (**Figure 6a**). This is attributed to the exhalation and inhalation signals not crossing the x-axis at the exact same time point, causing negative values under the square root in Equation 3 when the inhalation signal is expected to be positive but is still negative. This could be a result of fluid transition delay, or also on the response time of the sensors.

For deep breathing cycles in **Figure 6b**, the subject was instructed to deliberately exhale forcefully, resulting in more controlled air flow. As such, the flow volume loops derived from deep breathing measurements tended to meet at the start and end points, with more similarities across multiple measurement cycles (resulting in overlapping loops). The average peak flow rate of the deep breathing measurements in **Figure 6b** was 4.028 ± 0.295 L s^{-1}. We compared this value with a commercial peak flow meter (Microlife PF100), obtaining an average peak flow rate ($n = 10$) of 3.800 ± 0.399 L s^{-1} (**Table S1**). Our spirometer only measured the change in the pressure due to flow, and thus could not quantify absolute residual volume (i.e. lung capacity), which is typically 1 to 1.2 L in healthy adults.[40] However, it is possible that the difference between the inhalation and exhalation volume was in part due to the relative change in residual volume.

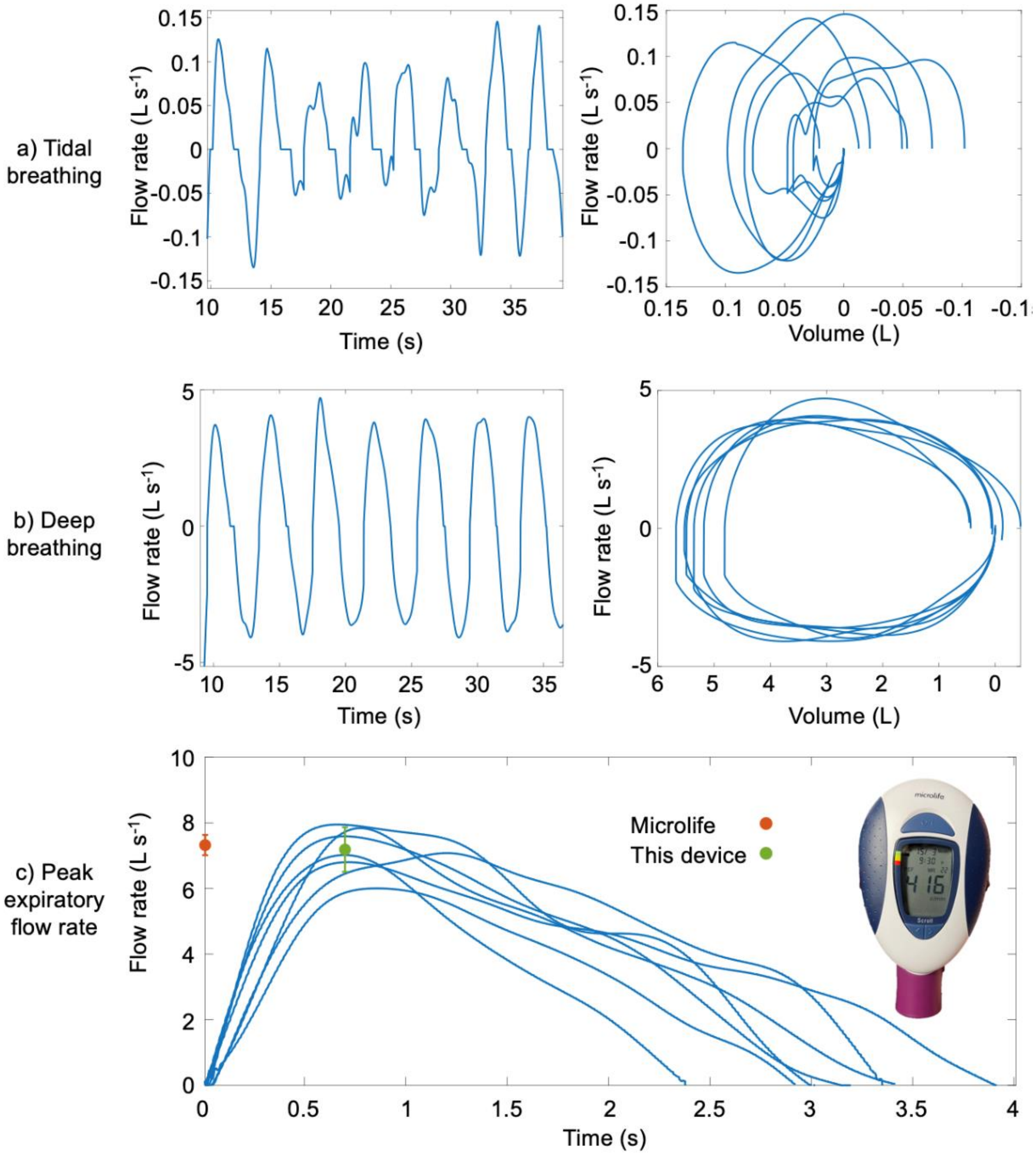

Figure 6. Flow volume loops. Each row shows measurements for each of the 3 types of breathing exercises recorded: **a)** tidal breathing (row 1), **b)** deep breathing (row 2), and **c)** PEFR measurement (row 3). The right plots in a) and b) depicts flow volume loops calculated from the flow rate plots (left). The PEFR measurement plot depicts 7 individual measurements. The average PEFR value is shown in green for the 7 measurements taken on our bidirectional venturi spirometer and compared to values measured by a commercial peak flow meter (orange) and shown in the inset photograph.

The PEFR measurement (**Figure 6c**) recorded the highest flow rate that could be forcibly exhaled after taking the deepest breath possible. It is different from deep breathing in that it is generally recorded in 1 cycle increments and requires an exhale at the highest possible velocity.[4] From PEFR measurements, we obtained an average PEFR ($n = 7$) of 7.187 ± 0.679 L s^{-1} for the female subject. This value was checked against the commercial peak flow meter used by the same individual and and determined to be within the same range (7.32 ± 0.31 L s^{-1} in the peak flow meter) (**Table S1)**. Both of these measurements were consistent with typical PEFR values for women (5.3-7.8 L s^{-1})[41]. For reference, PEFR values for men typically range between 7.5-9.2 L s^{-1}.

Flow resistance was measured without fudge factors across all breathing types and yielded values of 49.51 +/- 4.04 Pa L^{-1} s^{-1} , 32.07 +/- 1.11 Pa L^{-1} s^{-1} , and 14.83 +/- 2.53 Pa L^{-1} s^{-1} for PEFR, deep breathing, and tidal breathing, respectively. Flow resistance requirements by the American Thoracic Society are less than 49 Pa L^{-1} s^{-1} for 0-14 L s^{-1}[42]. The overall flow measurement range of the device in this study ranged from 0.1 L s^{-1} to 7.96 L s^{-1} . We calculated an average standard deviation of sensor noise to be 0.037 pF. With a limit of detection criterion of an SNR of 3:1, this yields a device limit of detection of 0.09 pF. The above measurements demonstrated the capability of a bidirectional venturi spirometer to provide detailed flow rate information for both tidal and deep breathing, as well as PEFR values consistent with peak flow meter devices.

Conclusion

In this work, we demonstrate a venturi flow meter capable of measuring respiratory flow in two directions, for inhalation and exhalation, using capacitive foam sensors. We show that the bidirectional spirometer is capable of monitoring the flow rate continually for both tidal and deep breathing and obtained a useful metric (PEFR) for evaluating human lung function. The spirometer was made from a 3D printed resin body and capacitive foam sensors, and thus is both low cost and highly portable. Simulations using FEA and experimental testing validate the use of a symmetric design for measuring both positive (exhalation) and negative (inhalation) respiratory flow using one device.

Future work entails multiple human subjects' evaluations to characterize the variability accross individuals. From a design aspect, the pressure and flow rate correction factors (S_p and S_f, respectively) likely arise from the use of an acoustics module in the FEA simulations, as this module does not calculate turbulent flow and assumes no viscous forces are in effect. As such, simulations calculate much lower pressure values compared to experimental measurements. Future improvements to this venturi spirometer could be made possible by more detailed simulations to analyze the flow separation over time during breathing cycles, to determine the cause of the correction factor and potentially eliminate it. Another potential aspect for optimization is the length of the spirometer tube. Our calculations suggest that the distance from the inlet to the first sensor necessary to guarantee a fully developed flow would require a tube that is at least 29 cm long.[43] For practical use of the device, we chose a much shorter distance (9.95 cm), which likely caused some flow separation during measurements (explanation in supporting information). Thus, future geometry optimizations can be applied to ensure fully developed flow in the sensing regions. With improvements to device design and performance, other useful spirometric indices could likely be derived from breathing measurements, such as forced expiratory volume after 1 second (FEV1) and forced vital capacity (FVC). Overall, the low-cost, portable spirometer design we demonstrate here offers the potential to increase access to lung function testing. While future work is needed to examine the reliability issues of the device for point-of-care monitoring of respiratory illnesses, the compactness and ease of manufacture make our design amenable to rapid prototyping and validation.

Acknowledgements

This research was supported by Center for Wearable Sensors (CWS) at UC San Diego. L.L.B. acknowledges the support provided by the National Science Foundation Graduate Research Fellowship Program under Grant DGE-2038238 and by the Achievement Rewards for College Scientists (ARCS) Foundation. I.F. acknowledges support from the Department of Defense (DoD) through the National Defense Science & Engineering Graduate (NDSEG) Fellowship Program. A.X.C. acknowledges support from the UC President's Dissertation Year Fellowship. D.J.L. acknowledges support from the National Science Foundation under award CBET-2223566. T.N.N. acknowledges support from the National Science Foundation under award CBET-2054517.

Conflict of Interest

The authors declare no conflict of interest.

Ethical Committee Approval

The testing of this device was covered under Institutional Review Board study #804551 at the University of California, San Diego. Informed consent was obtained from the subject in this study.

Data Availability Statement

The data is available in this Mendeley repository:

https://data.mendeley.com/datasets/fzh8pr6png/1

References

(1) Hoesterey, D.; Das, N.; Janssens, W.; Buhr, R. G.; Martinez, F. J.; Cooper, C. B.; Tashkin, D. P.; Barjaktarevic, I. Spirometric Indices of Early Airflow Impairment in Individuals at Risk of Developing COPD: Spirometry beyond FEV1/FVC. *Respiratory Medicine* **2019**, *156* (August), 58–68. https://doi.org/10.1016/j.rmed.2019.08.004.

(2) Yawn, B. P.; Enright, P. L.; Lemanske, R. F.; Israel, E.; Pace, W.; Wollan, P.; Boushey, H. Spirometry Can Be Done in Family Physicians’ Offices and Alters Clinical Decisions in Management of Asthma and COPD. *Chest* **2007**, *132* (4), 1162–1168. https://doi.org/10.1378/chest.06-2722.

(3) McCormack, M.; Kaminsky, D. *Pulmonary Function Laboratories: Advice Regarding COVID-19*. https://www.thoracic.org/professionals/clinical-resources/disease-related-resources/pulmonary-function-laboratories.php (accessed 2022-08-02).

(4) Graham, B. L.; Steenbruggen, I.; Barjaktarevic, I. Z.; Cooper, B. G.; Hall, G. L.; Hallstrand, T. S.; Kaminsky, D. A.; McCarthy, K.; McCormack, M. C.; Miller, M. R.; Oropez, C. E.; Rosenfeld, M.; Stanojevic, S.; Swanney, M. P.; Thompson, B. R. Standardization of Spirometry 2019 Update an Official American Thoracic Society and European Respiratory Society Technical Statement. *American Journal of Respiratory and Critical Care Medicine* **2019**, *200* (8), E70–E88. https://doi.org/10.1164/rccm.201908-1590ST.

(5) Gulla, K. M.; Kabra, S. K. Peak Expiratory Flow Rate as a Monitoring Tool in Asthma. *Indian J Pediatr* **2017**, *84* (8), 573–574. https://doi.org/10.1007/s12098-017-2398-x.

(6) Patil, R.; N, S.; Veena, V. Peak Flow Meter and Digital Spirometer: A Comparative Study of Peak Expiratory Flow Rate Values. *National Journal of Physiology, Pharmacy and Pharmacology* **2020**, *10* (0), 1–1. https://doi.org/10.5455/njppp.2020.10.02047202004052020.

(7) Fung, A. G.; Tan, L. D.; Duong, T. N.; Schivo, M.; Littlefield, L.; Delplanque, J. P.; Davis, C. E.; Kenyon, N. J. Design and Benchmark Testing for Open Architecture Reconfigurable Mobile Spirometer and Exhaled Breath Monitor with GPS and Data Telemetry. *Diagnostics* **2019**, *9* (3), 1–12. https://doi.org/10.3390/diagnostics9030100.

(8) Rondinel, T. Z.; Corrêa, I. F.; Hoscheidt, L. M.; Bueno, M. H.; Silva, L. M. C. da; Reppold, C. T.; Dal Lago, P. Incentive Spirometry Combined with Expiratory Positive Airway Pressure Improves Asthma Control and Quality of Life in Asthma: A Randomised

Controlled Trial. *Journal of Asthma* **2015**, *52* (2), 220–226. https://doi.org/10.3109/02770903.2014.956890.

(9) Bastin, R.; Moraine, J.-J.; Bardocsky, G.; Kahn, R.-J.; Mélot, C. Incentive Spirometry Performance. *Chest* **1997**, *111* (3), 559–563. https://doi.org/10.1378/chest.111.3.559.

(10) Sinharay, A.; Rakshit, R.; Khasnobish, A.; Chakravarty, T.; Ghosh, D.; Pal, A. The Ultrasonic Directional Tidal Breathing Pattern Sensor: Equitable Design Realization Based on Phase Information. *Sensors (Switzerland)* **2017**, *17* (8). https://doi.org/10.3390/s17081853.

(11) Koutsis, T.; Pikasis, P.; Psyrris, A.; Kaltsas, G. A Thermal Flow Sensor with a 3D Printed Housing for Spirometry Applications. *Microelectronic Engineering* **2020**, *226* (March), 111286. https://doi.org/10.1016/j.mee.2020.111286.

(12) Beyaz, M. I.; Habibiabad, S.; Yildiz, H.; Goreke, U.; Azgin, K. A Turbine-Based MEMS Sensor for Spirometry with Wearable Devices. *IEEE Sensors Journal* **2019**, *19* (19), 8612–8617. https://doi.org/10.1109/JSEN.2019.2919599.

(13) Yoshida, T.; Hamada, Y.; Nakamura, S.; Kurihara, Y.; Watanabe, K. Spirometer Based on Vortex Whistle to Monitor Lung Disorders. *IEEE Sensors J.* **2022**, *22* (11), 11162–11172. https://doi.org/10.1109/JSEN.2022.3170314.

(14) Carspecken, C. W.; Arteta, C.; Clifford, G. D.; Engineering, B.; Science, E. TELESPIRO : A LOW-COST MOBILE SPIROMETER FOR RESOURCE-LIMITED SETTINGS Department of Medical Education , Harvard Medical School , Boston MA , United States. *Point-of-Care Healthcare Technologies (PHT), 2013 IEEE* **2013**, 16–18.

(15) Adamski, K.; Kawa, B.; Walczak, R. 3D Printed Flowmeter Based on Venturi Effect with Integrated Pressure Sensors. *Proceedings* **2018**, *2* (13), 1509. https://doi.org/10.3390/proceedings2131509.

(16) Zhou, B.; Costa, A. B.; Lukowicz, P. Accurate Spirometry with Integrated Barometric Sensors in Face-Worn Garments. *Sensors (Switzerland)* **2020**, *20* (15), 1–22. https://doi.org/10.3390/s20154234.

(17) Zhang, B.; Tang, Y.; Dai, R.; Wang, H.; Sun, X.; Qin, C.; Pan, Z.; Liang, E.; Mao, Y. Breath-Based Human–Machine Interaction System Using Triboelectric Nanogenerator. *Nano Energy* **2019**, *64*, 103953. https://doi.org/10.1016/j.nanoen.2019.103953.

(18) Wang, M.; Zhang, J.; Tang, Y.; Li, J.; Zhang, B.; Liang, E.; Mao, Y.; Wang, X. Air-Flow-Driven Triboelectric Nanogenerators for Self-Powered Real-Time Respiratory Monitoring. *ACS Nano* **2018**, *12* (6), 6156–6162. https://doi.org/10.1021/acsnano.8b02562.

(19) Alvarez, J. C.; Raymundo, C.; Zapata, G.; Ronceros, J.; Flores, M.; Ruiz, F. Patented Portable Spirometer Based on Fluid Mechanics and Low Energy Consumption to Monitor Rehabilitation of Covid-19 Patients. *Energy Reports* **2020**, *6* (June), 179–188. https://doi.org/10.1016/j.egyr.2020.08.042.

(20) Carta, R.; Turgis, D.; Hermans, B.; Jourand, P.; Onclin, R.; Puers, R.; Leuven, K. U. A Differential Pressure Approach to Spirometry. *Conference Proceedings - IEEE Biomedical Circuits and Systems Conference Healthcare Technology, BiOCAS2007* **2007**, 5–8. https://doi.org/10.1109/BIOCAS.2007.4463295.

(21) Sridevi, P.; Kundu, P.; Islam, T.; Shahnaz, C.; Fattah, S. A. A Low-Cost Venturi Tube Spirometer for the Diagnosis of COPD. *IEEE Region 10 Annual International Conference, Proceedings/TENCON* **2019**, *2018-Octob* (October), 723–726. https://doi.org/10.1109/TENCON.2018.8650092.

(22) Zhang, J. X. Analysis on the Effect of Venturi Tube Structural Parameters on Fluid Flow. *AIP Advances* **2017**, *7* (6). https://doi.org/10.1063/1.4991441.

(23) Tsirlis, M.; Michailidis, N. Low-Pressure Gas Atomization of Aluminum through a Venturi Nozzle. *Advanced Powder Technology* **2020**, *31* (4), 1720–1727. https://doi.org/10.1016/j.apt.2020.02.011.

(24) Latif, L.; Macdonald, J. Suction Devices. *Anaesthesia and Intensive Care Medicine* **2018**, *19* (1), 16–19. https://doi.org/10.1016/j.mpaic.2017.10.010.

(25) Wegel, R. L.; Riez, R. R. Measurement of the Constants of a Single Reed Wind Vibrator. *The Journal of the Acoustical Society of America* **1930**, *1* (2A), 171–171. https://doi.org/10.1121/1.1901893.

(26) Soto-Ruiz, K. M.; Peacock, W. F.; Varon, J. The Men and History behind the Venturi Mask. *Resuscitation* **2011**, *82* (3), 244–246. https://doi.org/10.1016/j.resuscitation.2010.11.016.

(27) Titheradge, P.; Robergs, R. Static and Dynamic Performance of a Venturi Airflow Sensor. *Flow Measurement and Instrumentation* **2020**, *73* (July 2019), 101725. https://doi.org/10.1016/j.flowmeasinst.2020.101725.

(28) Mitchell, V.; Cheesman, K. Gas, Tubes and Flow. *Anaesthesia and Intensive Care Medicine* **2010**, *11* (1), 32–35. https://doi.org/10.1016/j.mpaic.2009.10.010.

(29) Rapp, B. E. Fluids. In *Microfluidics: Modelling, Mechanics and Mathematics*; Elsevier, 2017; pp 243–263. https://doi.org/10.1016/B978-1-4557-3141-1.50009-5.

(30) Cortés, S.; Güemes, D.; Ávila, R. Low Reynolds Number Flow Around a Flying Saucer Micro Air Vehicle. *COMSOL Conference* **2013**, 1–7.

(31) Mhetre, M. R.; Abhyankar, H. K. Human Exhaled Air Energy Harvesting with Specific Reference to PVDF Film. *Engineering Science and Technology, an International Journal* **2017**, *20* (1), 332–339. https://doi.org/10.1016/j.jestch.2016.06.012.

(32) Hermann Schlichting. *Boundary Layer Theory*, 7th ed.; McGraw-Hill: New York, 1979.

(33) Katopodes, N. D. *Viscous Fluid Flow*; 2019. https://doi.org/10.1016/b978-0-12-815489-2.00005-8.

(34) Russo, M. A.; Santarelli, D. M.; O'Rourke, D. The Physiological Effects of Slow Breathing in the Healthy Human. *Breathe* **2017**, *13* (4), 298–309. https://doi.org/10.1183/20734735.009817.

(35) Zhai, Y.; Wang, Z.; Kwon, K.; Cai, S.; Lipomi, D. J.; Ng, T. N. Printing Multi-Material Organic Haptic Actuators. *Adv. Mater.* **2021**, *33* (19), 2002541. https://doi.org/10.1002/adma.202002541.

(36) Mansour, E.; Vishinkin, R.; Rihet, S.; Saliba, W.; Fish, F.; Sarfati, P.; Haick, H. Measurement of Temperature and Relative Humidity in Exhaled Breath. *Sensors and Actuators B: Chemical* **2020**, *304*, 127371. https://doi.org/10.1016/j.snb.2019.127371.

(37) Azarnoosh, J.; Sreenivas, K.; Arabshahi, A. CFD Investigation of Human Tidal Breathing through Human Airway Geometry. *Procedia Computer Science* **2016**, *80*, 965–976. https://doi.org/10.1016/j.procs.2016.05.392.

(38) Pleil, J. D.; Ariel Geer Wallace, M.; Davis, M. D.; Matty, C. M. The Physics of Human Breathing: Flow, Timing, Volume, and Pressure Parameters for Normal, on-Demand, and Ventilator Respiration. *J. Breath Res.* **2021**, *15* (4), 042002. https://doi.org/10.1088/1752-7163/ac2589.

(39) Titheradge, P.; Robergs, R. Static and Dynamic Performance of a Venturi Airflow Sensor. *Flow Measurement and Instrumentation* **2020**, *73* (July 2019), 101725–101725. https://doi.org/10.1016/j.flowmeasinst.2020.101725.
(40) Lofrese, J. J.; Tupper, C.; Denault, D.; Lappin, S. L. Physiology, Residual Volume. In *StatPearls*; StatPearls Publishing: Treasure Island (FL), 2022.
(41) R, S. The Peak Expiratory Flow Rate (PEFR): The Effect of Stress in a Geriatric Population of Chennai- A Pilot Study. *JCDR* **2013**. https://doi.org/10.7860/JCDR/2013/5356.2728.
(42) Johns, D. P.; Ingram, C. M.; Khov, S.; Rochford, P. D.; Walters, E. H. Effect of Breathing Circuit Resistance on the Measurement of Ventilatory Function. *Thorax* **1998**, *53* (11), 944–948. https://doi.org/10.1136/thx.53.11.944.
(43) Çengel, Y. A.; Cimbala, J. M. *Fluid Mechanics: Fundamentals and Applications*, Fourth edition.; McGraw-Hill Education: New York, NY, 2018.

Table of Contents text

In this work, flexible capacitive foam sensors were used to measure inspired and expired air from a human. Using a 3D printed tube, we obtained flow rate and volume measurements for tidal and deep breathing, and peak expiratory flow rate measurement, using differential pressure signals from the sensors embedded into the spirometer walls.